

iVINE - Ionization in the parallel tree/SPH code VINE: First results on the observed age-spread around O-stars

M. Gritschneider^{1*}, T. Naab¹, A. Burkert¹, S. Walch¹, F. Heitsch², M. Wetzstein³

¹ *Universitäts-Sternwarte München, Scheinerstr.1, D-81679 München, Germany*

² *Department of Astronomy, University of Michigan, Michigan, United States*

³ *Department of Astrophysical Sciences, Princeton University, Princeton, United States*

Accepted ????. Received ??? in original form ???

ABSTRACT

We present a three-dimensional, fully parallelized, efficient implementation of ionizing UV radiation for smoothed particle hydrodynamics (SPH) including self-gravity. Our method is based on the SPH/tree code VINE. We therefore call it iVINE (for Ionization + VINE). This approach allows detailed high-resolution studies of the effects of ionizing radiation from e.g. young massive stars on their turbulent parental molecular clouds. In this paper we describe the concept and the numerical implementation of the radiative transfer for a plane-parallel geometry and we discuss several test cases demonstrating the efficiency and accuracy of the new method. As a first application, we study the radiatively driven implosion of marginally stable molecular clouds at various distances of a strong UV source and show that they are driven into gravitational collapse. The resulting cores are very compact and dense exactly as it is observed in clustered environments. Our simulations indicate that the time of triggered collapse depends on the distance of the core from the UV source. Clouds closer to the source collapse several 10^5 years earlier than more distant clouds. This effect can explain the observed age spread in OB associations where stars closer to the source are found to be younger. We discuss possible uncertainties in the observational derivation of shock front velocities due to early stripping of proto-stellar envelopes by ionizing radiation.

Key words: ISM: H II regions – ISM: kinematics and dynamics – radiative transfer – ultraviolet: ISM – stars: formation – methods: numerical

1 INTRODUCTION

As hydrodynamical simulations become more and more advanced one of the key issues is the successful implementation of additional physics like the effects of radiation. Prominent applications are for example the reionization of the early universe (for a comparison of methods see Iliev et al. 2006 and references therein).

In our present day universe ionizing radiation still plays a vital role. UV-radiation from massive, young stars ionizes their surrounding. The hot, ionized gas then expands into the cold, neutral gas and thus drives shock fronts into the parental molecular clouds. Up to now it is not fully understood if this violent feedback enhances or hinders star formation. Elmegreen & Lada (1977) proposed that the shock front builds up dense regions by sweeping up the cold gas, which then eventually collapse due to gravitational instability and form stars. This is called the ‘collect and collapse model’ (see also the review by Elmegreen 1998). Another sit-

uation arises when preexisting, dense structures (e.g. molecular cloud cores) that are gravitationally marginally stable get compressed by the approaching front and start collapsing. This is commonly called radiation driven implosion (see e.g. Sandford et al. 1982).

Observations provide widespread evidence for these scenarios (Sugitani et al. 1989, Hester et al. 1996). More recent observations indicate triggered star formation on the edges of HII-regions e.g. in the Orion clouds (Stanke et al. 2002), the Carina nebula (Smith et al. 2000), M16 (Fukuda et al. 2002), M17 (Jiang et al. 2002), 30 Dor (Walborn et al. 2002) and the SMC (Gouliermis et al. 2007). Deharveng et al. (2005) report triggered star formation in samples of more distant HII regions. Besides these quite complex large scale regions there have been numerous observations of bright rimmed cometary globules. These are small isolated clouds with a clear head to tail structure with the dense heads pointing towards an ionizing source (Sugitani et al. 1991). Their morphology enables a direct comparison to simulations. In particular, the properties of individual young stellar objects (YSOs) surrounding OB-associations can be deter-

* E-mail: gritschm@usm.uni-muenchen.de

mined precisely. YSOs are observed in the mass range from T Tauri ($0.1 - 3M_{\odot}$) up to Herbig Ae Be ($2 - 8 M_{\odot}$) stars (see e.g. Lee & Chen 2007, Snider et al. 2007). The velocity of the shock front triggering the star formation is calculated from the age difference of the stars and their relative distance. These estimates are in the range of a few km/s (e.g. Thompson et al. 2004, Getman et al. 2007).

Numerous simulations on the topic of cloud evaporation and sequential star formation have been performed. Yorke et al. (1982) (and references therein) published a series of two-dimensional simulations on the gas dynamics of HII-regions, especially on champagne flows, where a stream of hot gas breaks through the border of cold, confining gas. Subsequently, Elmegreen et al. (1995) presented two-dimensional, grid-based simulations showing that the expansion of an HII-region into the surrounding cloud can trigger star formation. Kessel-Deynet & Burkert (2003) demonstrated with a three-dimensional SPH code, that a marginally stable molecular cloud core can be triggered into collapse when exposed to strong UV radiation. With a more detailed description of radiation implemented into an SPH code Miao et al. (2006) could reproduce the observed features of the Eagle Nebula, including the photodissociation regions and the temperature profile. Using a three-dimensional grid-based scheme, Mellema et al. (2006) simulated the HII-region excavated by a point source of UV-radiation. They find remarkably similar morphologies and physical properties when comparing their models to observations. Furthermore simulations with an SPH-code by Dale et al. (2005) and a grid code by Mac Low et al. (2007) showed that a turbulent interstellar medium surrounding an O-star allows the ionizing radiation to efficiently expel most of the nearby gas. Only the denser regions resist and continue to collapse.

However none of the authors so far described ionizing radiation as an efficient trigger for star formation. There is only weak evidence by Dale et al. (2007), that the external irradiation of a collapsing cloud by a point source can indeed increase the star formation efficiency from 3% to 4% when compared to a control run without radiation. For a review of feedback processes we refer the reader to Mac Low (2007). For completeness we would like to refer to recently published implementations for ionizing radiation into an SPH code by Pawlik & Schaye (2008), where the photons of a source are followed along cones, and Altay et al. (2008), where the radiation is followed via a Monte Carlo ray-tracing scheme.

All these studies demonstrate that there is a strong connection between the UV-radiative feedback from massive stars and the observed morphologies of the ambient molecular cloud gas. Yet, a quantitative discussion of the interaction between UV-radiation and turbulent molecular clouds is still missing. To advance our understanding, we introduce iVINE, the fully parallel implementation of UV-radiation in the parallel tree-SPH-code VINE (Wetzstein et al. 2008, Nelson et al. 2008). This efficient tool permits high resolution simulations of molecular clouds in the vicinity of strong UV sources such as an O-star or association.

The paper is structured as follows. The physical model and its implementation are described in Section 2, followed by a detailed comparison of the scheme with analytical results (Sec. 3). We apply the new method to the radiatively driven implosion of a marginally stable molecular cloud core

and compare three simulations with different initial UV fluxes to observations (Sec 4). In Section 5 we summarize and discuss the results.

2 NUMERICAL METHOD

As soon as a young massive star emits UV-radiation it ionizes its surrounding, creating a HII-region. Initially the ionization proceeds fast with a speed of this rarefied (or R-type) front of $v_R \gg a_{\text{hot}}$, where a_{hot} is the sound speed of the hot, ionized gas. After a sound crossing timescale the hot gas reacts to its increased temperature and an isothermal shock front is driven into the cold surrounding medium. This dense (or D-type) shock travels at a much smaller speed $v_D \approx a_{\text{hot}}$. For a full textbook analysis of this evolution see e.g. Osterbrock (1989).

2.1 Prescription of ionizing radiation

To follow the evolution of the HII-region of a young massive star in a numerical simulation we use a prescription for the ionizing UV-radiation similar to the one proposed by Kessel-Deynet & Burkert (2000) as presented before (Gritschneder et al. 2007). The flux J at any given position x is given by

$$J(x) = J_{\text{Ly}} e^{-\tau_{\nu}(x)}, \quad (1)$$

where J_{Ly} is the Lyman continuum flux of the hot star. The optical depth τ_{ν} is given by the integral along the line of sight between the source of radiation and the position x

$$\tau_{\nu} = \int_0^x \kappa_{\nu} \rho dx, \quad (2)$$

where κ_{ν} is the frequency weighted absorption coefficient

$$\kappa_{\nu} = \frac{\sigma_{\nu} n_{\text{H}}}{\rho}, \quad (3)$$

with n_{H} being the number density of neutral hydrogen and ρ the mass density of the gas. We assume the gas is pure hydrogen with a mean molecular weight of $\mu = 1$. As the frequency dependent absorption cross section σ_{ν} peaks at the Lyman break it is a valid assumption to take an average cross section $\bar{\sigma}$, thereby approximating the radiation to be monochromatic. Thus, every photon above the Lyman break is assumed to ionize one hydrogen atom.

We define the ionization degree η as

$$\eta = \frac{n_e}{n}, \quad (4)$$

where n_e is the number density of electrons and n is the combined number density of protons and neutral hydrogen atoms. The time derivative of the ionization degree can be written as

$$\frac{d\eta}{dt} = \frac{1}{n} \frac{dn_e}{dt} = \frac{1}{n} (I - R), \quad (5)$$

with the ionization rate I given as

$$I = \nabla J \quad (6)$$

and the recombination rate R as

$$R = n_e^2 \alpha_{\text{B}} = \eta^2 n^2 \alpha_{\text{B}}. \quad (7)$$

For the recombination coefficient α_B we choose

$$\alpha_B = \sum_{i=2}^{\infty} \alpha_i, \quad (8)$$

where α_i is the recombination probability for a level i of the hydrogen atom. The recombination of electrons and protons leads to a diffuse field of Lyman continuum photons, which in turn can again ionize a hydrogen atom. We neglect this effect under the assumption that every reemitted photon is in turn immediately absorbed in the direct surrounding. This assumption, called ‘on the spot approximation’ is valid as long as the hydrogen density is high enough (e.g. Spitzer 1978), which is always true in the vicinity of the ionization front. Some fraction of the UV-photons is absorbed by dust, and re-emitted in the IR-regime, leading to an effective lower flux. We neglect this effect, since the flux incident on the simulation volume is determined largely by its distance from the radiation source, so that geometrical dilution of the radiation field is likely to be more important than absorption by dust.

The average temperature of the gas is coupled linearly to the ionization degree η through

$$T = T_{\text{hot}} \cdot \eta + T_{\text{cold}} \cdot (1 - \eta), \quad (9)$$

where T_{cold} is the initial temperature of the cold, unionized gas and T_{hot} is the average temperature of the ionized gas.

2.2 Implementation

To treat the hydrodynamical and gravitational evolution of the gas we use the parallel smoothed particle hydrodynamics (SPH) code called VINE developed by Wetzstein et al. (2008) and Nelson et al. (2008). SPH is a Lagrangian method, which renders it extremely suitable to cover several orders of magnitude in density and spatial scale, for example during cloud core collapse and star formation. VINE is a powerful parallel implementation of the SPH method in combination with a tree code for the calculation of gravitational forces. It offers a Runge-Kutta integrator as well as a Leapfrog integrator. Both schemes can be used in combination with individual particle time-steps. For this work the Leapfrog integrator is chosen. Every time the equation of state is computed we calculate the ionization degree for all particles in the entire simulation.

The heating by UV-radiation can be treated as decoupled from the dynamic evolution since the recombination timescale

$$t_{\text{rec}} = \frac{1}{n\alpha_B} \quad (10)$$

is much shorter than any hydrodynamical timescale. In our simulations (see Section 4) the crossing time even in the hot gas is $t_{\text{hot}} \approx 70\text{kyr}$, whereas the recombination timescale is $t_{\text{rec}} \approx 1\text{kyr}$ for a number density of $n = 100\text{cm}^{-3}$. Thus, it is valid to treat ionization and hydrodynamics as two separate processes. In other words the ionization can be assumed to happen instantaneously. Frequently updating the ionization degree together with a modified time-step criterion (see Section 2.3) ensures that the radiation is treated correctly on all scales.

To include the effect of UV-radiation we assume a plane-parallel geometry, i.e. parallel rays. This is valid as long as

the distance from the source of radiation is larger than the dimensions of the area of infall. In our simulations the radiation is impinging from the left hand side, that is from the negative x -direction. To couple ionization to hydrodynamics we use a ray-shooting algorithm. As the ionizing flux is propagated along the x -direction, we ensure the conservation of flux by dividing the (y, z) -plane into sub-domains of equal size, whose extent along the x -direction spans the whole simulation domain. Along each of these sub-domains or rays the flux is transported in a conservative manner. To convert the SPH-particle density ρ_{part} correctly into a gas density distribution within these three-dimensional rays the volume and thus the diameter d_{part} that each SPH-particle occupies is calculated via the mass of each particle m_{part} :

$$d_{\text{part}} = 2 \cdot \left(\frac{3}{4\pi} \frac{m_{\text{part}}}{\rho_{\text{part}}} \right)^{1/3}. \quad (11)$$

The width Δy and the height Δz of the rays or bins is then set to the average value \bar{d}_{part} of the particles closest to the source. To determine this value the first two particles in each ray at the previous time-step are taken into account. Since this is the region with the lowest density throughout the entire simulation this guarantees that the bin-size is always larger than the characteristic particle resolution. As soon as the ray approaches a density increase the local d_{part} becomes smaller than Δy and Δz . For

$$\frac{d_{\text{part}}}{\Delta y} = \frac{d_{\text{part}}}{\Delta z} < \frac{1}{2} \quad (12)$$

we refine the ray subsequently into four sub-rays to treat the ionization of high density regions correctly. Each of the sub-rays inherits the optical depth of the main ray. Currently the code allows for five levels of refinement, thus increasing the effective bin resolution in each direction by a factor of 32. In principle it would be possible to de-refine the sub-rays by using the average optical depth of the four refined sub-rays for the de-refined bin. We do not include this, since it would lead to an unphysical shading of lower density sub-rays as soon as they are combined with a high density sub-ray due to an overestimation of the optical depth.

To calculate the optical depth, we sort the particles within each bin according to their distance to the source and discretize into subsections of the size

$$\Delta x_i = \frac{x_{i+1} - x_{i-1}}{2}. \quad (13)$$

Thus, Δx_i is the projected distance of a particle i to its direct neighbours closer and further away from the source, i.e. the length along the line of sight the particle occupies. We then calculate the optical depth τ along each ray by summing up the individual optical depths τ_i of each particle i . The discrete value of τ_i is given according to Eq. 2 as

$$\tau_i = \bar{\sigma} n_{\text{H},i} \Delta x_i. \quad (14)$$

The number density n_{H} and the density ρ used to calculate the recombination rate (cf Eq. 7) are simply given by the SPH-density ρ_{part} . From these quantities the new ionization degree η is determined according to Eq. 2 by a Newton-Raphson iteration scheme. It converges with a precision of more than 0.1% in less than 200 iterations. When the ionization degree reaches a value of $\eta = 1 \times 10^{-10}$ we terminate the further calculation of this bin. This implementation is fully parallelized in OpenMP.

2.3 Modification of the time-step criterion

A detailed discussion of the different time-step criteria implemented in the underlying VINE code is given in Wetzstein et al. (2008). Note that our implementation of ionizing radiation is designed to be used in connection with individual particle time-steps (see Wetzstein et al. 2008, for details). To exactly follow the evolution of a particle during its ionization process it is vital to use a small enough time-step. To do so we decided to force every particle to a smaller time-step as soon as its ionization degree reaches $\eta > 10^{-3}$, i.e. when the particle is going to be ionized. The new time-step is chosen by a modified Courant-Friedrichs-Lewy (CFL) condition according to

$$\Delta t_{\text{new}} = a_{\text{cold}}/a_{\text{hot}} * \Delta t_{\text{CFL}}, \quad (15)$$

where a_{cold} and a_{hot} are the fixed respective sound-speeds of the cold and the ionized gas at T_{cold} and T_{hot} . Δt_{CFL} is the individual time-step the particle would get assigned due to the CFL-condition (see Wetzstein et al. 2008). This ensures that the hydrodynamical quantities are treated correctly even though the particle gets a boost in temperature. Therefore, we anticipate the subsequent acceleration due to the approaching ionization front by choosing already the much smaller time-step even though the particle is just ionized to 0.1%. This criterion also ensures that the ionization degree is followed accurately during the evolution of the later dense or D-type ionization front, because v_{D} is always smaller than the sound speed of the hot gas $v_{\text{D}} < a_{\text{hot}}$. Hence, this front will always be resolved by particles which have a small enough time-step to track the hot gas. In the beginning the evolution of the faster R-type front ($v_{\text{R}} \gg a_{\text{hot}}$) can be followed by using a small enough initial time-step since this phase is quite short ($\approx 5\text{kyr}$).

The choice of a small initial time-step together with the modified CFL-criterion ensure that the ionization degree η of a particle never changes by more than ± 0.1 per time-step in all of our simulations. Thus, the ionization front can be followed in both stages (R- and D-type) precisely.

3 NUMERICAL TESTS

In order to validate the algorithm we perform several tests. The first series of simulations addresses the evolution of the Strömgren solution and tests whether the time-dependent UV-flux is treated correctly on all scales. In addition, we demonstrate the correct implementation of the refinement (Section 3.1). The second series of simulations (Section 3.2) is designed to demonstrate the correct interaction of ionizing radiation and hydrodynamics. In the end the successful parallelization of the code is shown (Section 3.3).

3.1 Ionization without hydrodynamics

3.1.1 The Strömgren test - Ionization by a constant UV flux

When hydrodynamics is not taken into account, the homogeneous surrounding of an ionizing source will always converge towards an equilibrium between ionization and recombination. The volume of the ionized Strömgren sphere (Strömgren 1939) around an O-star is given by

$$V_{\text{S}} = \frac{J_{\text{Ly}}}{\alpha_{\text{B}} n^2}, \quad (16)$$

assuming a monochromatic source with a constant UV-flux J_{Ly} given in photons per second. α_{B} and n are again the recombination coefficient and the number density (for a textbook analysis see e.g. Shu 1991).

In the case of plane-parallel radiation, as discussed here, this volume is characterized by the length x_{s} , which can be penetrated by the ionizing radiation. x_{s} is determined by the surface S on which the photon flux per area and time, F_{Ly} , is impinging:

$$x_{\text{s}} = \frac{V_{\text{s}}}{S} = \frac{F_{\text{Ly}}}{\alpha_{\text{B}} n^2}. \quad (17)$$

The time evolution of the length $x_{\text{I}}(t)$ of this region is given by the differential equation

$$\frac{dx_{\text{I}}}{dt} n = F_{\text{Ly}} - x_{\text{I}}(t) \alpha_{\text{B}} n^2 \quad (18)$$

with the solution

$$x_{\text{I}}(t) = x_{\text{s}}(1 - e^{-t/t_{\text{rec}}}), \quad (19)$$

where $t_{\text{rec}} = 1/(n\alpha_{\text{B}})$ is the recombination or Strömgren timescale. The shape of the front is given by the ionization equilibrium equation

$$n(1 - \eta) \int_{\nu_{\text{Ly}}}^{\infty} F_{\nu} \sigma_{\nu} d\nu = n^2 \eta^2 \alpha_{\text{B}}, \quad (20)$$

which can be rewritten for the plane-parallel, monochromatic case in terms of the ionization degree (cf Eq. 4) as

$$\frac{d\eta}{dx} = \eta^2 \frac{1 - \eta}{1 + \eta} n \bar{\sigma} x_{\text{s}}. \quad (21)$$

This equation can be solved numerically and gives the ionization degree η at any given position x for the chosen number density n and mean cross-section $\bar{\sigma}$.

To test the code, we ran three simulations:

- Case A: 125k particles placed on a Cartesian grid
- Case B: 100k particles placed randomly
- Case C: 250k particles placed randomly

For cases B and C the particles are placed randomly in the simulation box and then are allowed to relax with periodic boundaries and the inclusion of hydrodynamics for one crossing timescale to dampen the numeric random noise. Thereafter we switch off the hydrodynamics and compute the ionization. For all simulations we used a mean density $n = 10\text{cm}^{-3}$. The simulated volume is $(2\text{pc})^3$, the length the ionization can penetrate is set to $x_{\text{s}} = 1\text{pc}$. The recombination coefficient and the absorption cross-section are set to typical values of $\alpha_{\text{B}} = 2.7 \times 10^{-13}\text{cm}^3\text{s}^{-1}$ and $\bar{\sigma} = 3.52 \times 10^{-18}\text{cm}^2$. For the above parameters, $F_{\text{Ly}} = 8.33 \times 10^7\text{photons cm}^{-2}\text{s}^{-1}$ and $t_{\text{rec}} = 11.8\text{kyr}$. The simulations run up to $t = 5t_{\text{rec}}$ to allow for a quasi-equilibrium state to evolve.

In Fig. 1 the time evolution of the penetration length $x_{\text{I}}(t)$ is shown. The position of the front is calculated by projection of the three-dimensional simulation along the y- and z-axis onto the x-axis. Note that the analytical solution (cf Eq. 19) is based on the idealized assumption that the medium is fully ionized ($\eta = 1.0$). However, the precise solution of Eq. 5 in equilibrium ($d\eta/dt = 0$) is

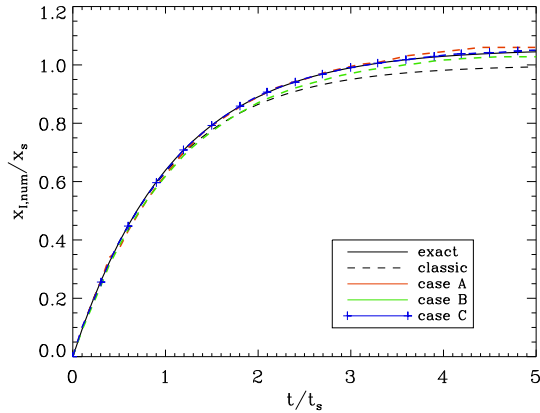


Figure 1. Time evolution of the ionization degree η for the three test cases with different particle numbers and distributions red (125k particles), green (100k particles) and blue (250k particles) lines. The black solid line denotes the exact solution, the black dashed line the classic (Strömgren) solution.

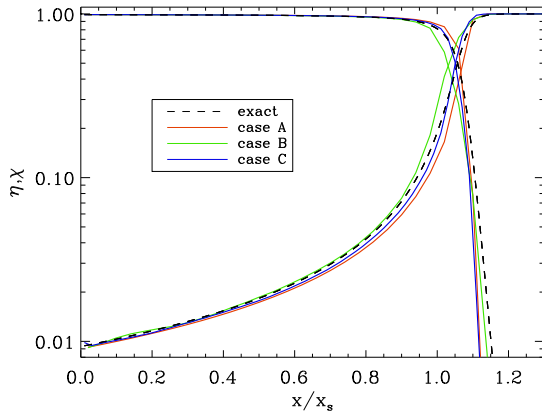


Figure 2. Ionization degree η (≈ 1 at $x/x_s = 0$) and neutral gas fraction $\chi = 1 - \eta$ versus position for the cases A (red), B (green) and C (blue). The dashed line represents the exact solution.

$$x_s \eta^2 = \frac{V_s}{S} = \frac{F_{Ly}}{\alpha_B n^2}. \quad (22)$$

In our simulations $x_s \eta^2 = 1\text{pc}$ is realized with $x_s = 1.05\text{pc}$ and $\eta = 0.976$. We call this the exact solution whereas the solution assuming $\eta = 1.0$ will be referred to as classic solution. Our simulations converge very well towards the exact solution. Case A, where the particles are initially placed on a grid, slightly overestimates the final value of x_s , while the low resolution simulation (case B) underestimates it. Nevertheless, already with only 100k this implementation shows a very good agreement with the analytical curve. In the high resolution simulation (case C) the numerical result lies right on top of the predicted line.

Fig. 2 shows the ionized fraction η and the neutral fraction $\chi = 1 - \eta$ after $t = 5t_s$ at the end of the simulation. The numerical solution of Eq. 21 is evaluated for the exact solution with a penetration length of $x_s = 1.05\text{pc}$. As expected from Fig. 1, case A overestimates the front position,

whereas case B underestimates it. Again the high resolution run C shows the best concordance and we can conclude that these results fit well within the range of the code comparisons done by Iliev et al. (2006). A more direct comparison to this work is not possible due to the plane-parallel nature of the test performed here.¹

3.1.2 Ionization by a time-varying source

A more challenging test is the treatment of a time-varying source of ionization. Although this situation is not very realistic for an O-star it nevertheless provides a very good method to test the treatment of a rapidly changing flux by the code.

To produce an ionization front that is traveling at a constant speed through a medium of constant density it is sufficient to increase the flux per area F_{Ly} linearly with time,

$$F_{Ly}(t) = nv_f + n^2 \alpha_B v_f t, \quad (23)$$

where v_f denotes the speed of the ionizing front. The first term on the right hand side provides the ionization of the front, while the second term compensates for the loss of flux due to recombinations on the way towards the front. We assume a constant density of $n = 10\text{cm}^{-3}$ and the velocity of the front is set at $v_f = 1.3 \times 10^5\text{cm s}^{-1}$. The other parameters are chosen as before.

Again the three initial conditions A, B and C from section 3.1.1 are explored. The results are shown in Fig. 3. As before the simulations match the theoretical solutions closely. In the beginning run A agrees very well with the solution. This is due to the very low numerical noise in the Cartesian grid. However, towards the end the low resolution leads to a deviation from the analytic value. In case B one can clearly see the effect of the noisy density distribution, since for the recombination R any error in the density leads to a quadratic error in the absorption of the photons (cf Eq. 7). Therefore, the position starts to oscillate around the exact position. This effect gets stronger the further the front penetrates, as more material has to be kept from recombining. Case C shows a very good agreement with the exact solution, the resolution is high enough to keep the noise in the density distribution low and thus the position of the front is followed precisely.

3.1.3 Testing the refinement - Ionization by a constant source in a two-density medium

All tests up to now were independent of the implementation of refinement, since in a constant density medium each particle occupies roughly the same diameter d_{part} (see Section 2.2). To verify the correct implementation of the refinement we set up a simulation with a two-density medium. A lower density gas phase with $n_1 = 10\text{cm}^{-3}$ is set up in the left half of the box and a higher density medium with $n_2 = 100\text{cm}^{-3}$

¹ Note that in Fig. 2 the neutral fraction χ converges towards a value of 10^{-2} at $x = 0\text{pc}$ in both the simulations and the exact solution whereas in Iliev et al. (2006) χ is reaching much lower values. This is due to the fact that in our simulations the irradiated surface stays constant whereas when simulating a point source this surface and thus χ can get infinitesimally small.

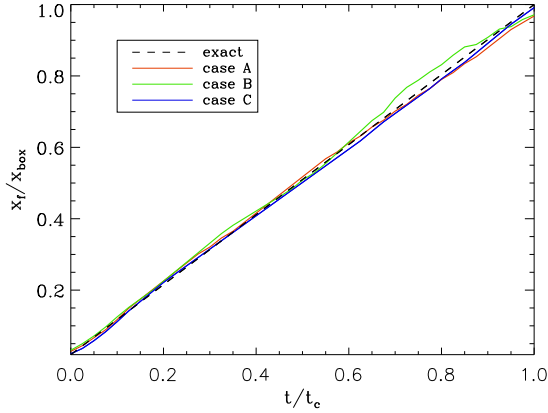


Figure 3. Numerical simulation of an ionization front that moves with constant speed through a medium of constant density. Plotted is the position of the front in units of the box length versus the time in units of the crossing time for the three cases A (red), B (green) and C (blue).

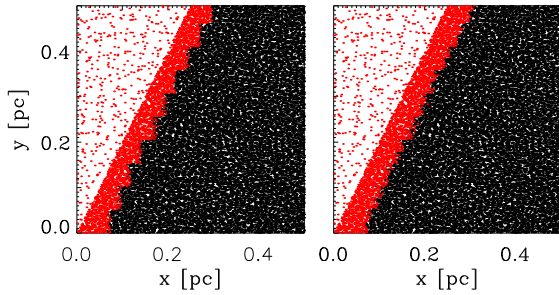


Figure 4. Effect of the refinement on a diagonal density step. Plotted are the SPH-particles in a $(0.5\text{pc})^3$ volume projected along the z -axis. Red: ionized particles ($\eta > 0.1$), black: unionized particles. Left: without the inclusion of refinement. Right: with the inclusion of one level of refinement.

is placed at the right half of the box. The density contrast is achieved via a different number of SPH-particles in the different regions, the particle masses are equal in the entire simulation. The required flux to ionize the simulation domain up to a position x_s can be calculated by linear superposition according to Eq. 22

$$F_{\text{Ly}} = \alpha_B x_1 n_1^2 + \alpha_B (x_s - x_1) n_2^2, \quad (24)$$

where $x_1 = 0.5\text{pc}$ is the extent of the low-density region. The simulation is set up with 550k randomly placed particles. The particle noise is reduced for both regions separately as described in Section 3.1.1. The penetration depth is set to $x_s = 1\text{pc}$. As soon as the equilibrium state is reached the numerically calculated penetration lengths are

$$x_{\text{eq,unrefined}} = 0.985 x_s \quad ; \quad x_{\text{eq,refined}} = 0.997 x_s \quad (25)$$

for the unrefined and the refined case. Very good agreement even with the unrefined code can be expected, as we always use the SPH-density in the calculation which is independent of the chosen bins for the calculation of the ionization and the recombination.

Nevertheless, the refinement has an important geometrical effect, which becomes clear when assuming a density contrast with a discontinuity which is not aligned vertical to the impinging radiation. We perform a test with a diagonal density contrast between two regions with a number density of $n_{\text{low}} = 10\text{cm}^{-3}$ and $n_{\text{high}} = 200\text{cm}^{-3}$ respectively. Again the particles are placed randomly and the noise is reduced (see Section 3.1.1). A cubic domain of $(0.5\text{pc})^3$ including 25k particles is shown in Fig. 4. In the unrefined case (left hand side) the effect of the original bin-size of $\approx 0.05\text{pc}$ can be clearly seen as step-like features. With refinement the density contrast of 20 leads to one level of refinement (since $d_{\text{part}}/\Delta y \approx 1/2.7$, cf Eq. 12) and the geometrical bias is already negligible (Fig. 4, right hand side). In the simulations in Section 4 all five levels of refinement lead to spatial resolution of the radiation in our simulations as high as 10^{-3}pc , therefore the radiation does not produce any unphysical geometrical effects.

3.2 Ionization with hydrodynamics

3.2.1 Steady propagation of an ionizing front

This test was originally proposed by Lefloch & Lazareff (1994). An area of constant density is ionized by a photon flux which increases linearly with time. This leads to a hydrodynamical shock wave traveling at a constant speed. The number densities n_i, n_c, n_0 in the ionized, the compressed and the undisturbed medium can then be calculated from the corresponding sound speeds a_i, a_c, a_0 . Let u_i be the speed of the ionization front and u_s be the speed of the shock front. The jump condition for a D-type ionization front can be written as

$$\frac{n_i}{n_c} = \frac{a_c^2}{a_i^2} = \frac{a_0^2}{a_i^2}, \quad (26)$$

since the compressed and the neutral medium have the same temperature and thus the same sound-speed. At the isothermal shock the jump conditions are

$$u_s(u_s - u_1) = a_0^2, \quad (27)$$

$$\frac{n_c}{n_0} = \frac{u_s^2}{a_0^2}, \quad (28)$$

where u_1 is the gas velocity just inside the shock. With the approximation of a thin shock it can be assumed that the ionization front and the shock front have the same speed $u_i = u_s$. For a detailed derivation of the jump conditions see e.g. Shu (1991). Introducing the time derivative of the ionizing flux $C = dF/dt$ the speed of the front can be calculated similar to Eq. 17:

$$u_i = \frac{C \alpha_B}{n_i^2} (= u_s). \quad (29)$$

The jump conditions can then be rewritten to give the following relations:

$$n_c = n_0 \frac{u_s^2}{a_0^2} = n_0 \left(\frac{C}{\alpha_B n_i^2 a_0} \right)^2 \quad (30)$$

$$n_i = n_c \frac{a_0^2}{a_i^2} = \left(\frac{n_0 C^2}{\alpha_B a_i^2} \right)^{\frac{1}{5}} \quad (31)$$

$$u_1 = u_s - \frac{a_0^2}{u_s}. \quad (32)$$

	Classic	Exact	Grid	SPHI	iVINE
n_c (cm $^{-3}$)	147	137	169	155	138 ± 6
n_i (cm $^{-3}$)	0.734	0.747	0.748	0.75	0.743 ± 0.01
u_i (km s $^{-1}$)	3.48	3.37	3.36	3.43	3.34 ± 0.18
u_1 (km s $^{-1}$)	3.24	3.12	-	-	3.13 ± 0.04

Table 1. Comparison of analytical and numerical results for the test including hydrodynamics and ionization. The iVINE data is obtained from the 2 million particle run, the errors given are 1σ . The grid data is taken from Lefloch & Lazareff (1994), the SPHI data from Kessel-Deynet & Burkert (2000). The analytical values differ from the previous work due to a higher accuracy in our calculations.

To compare directly to previous results, we used the initial conditions by Lefloch & Lazareff (1994). The density is $n_0 = 100\text{cm}^{-3}$, the temperature is $T_{\text{cold}} = 100\text{K}$. The flux increases linearly with time at a constant rate of $dF/dt = 5.07 \times 10^{-8}\text{cm}^{-2}\text{s}^{-2}$, starting from zero. As before the recombination parameter is set to $\alpha_B = 2.7 \times 10^{-13}\text{cm}^3\text{s}^{-1}$ and the ionized temperature is $T_{\text{hot}} = 10^4\text{K}$. Refinement is included.

The simulations are performed using the individual particle time-steps of VINE. For the determination of the time-step we use the criteria given in Wetzstein et al. (2008). Here we will only review briefly the parameters used. We use a combined time-step criterion based on the change in acceleration and velocity of the particle with an accuracy parameter of $\tau_{\text{acc}} = 1.0$. In addition, a CFL criterion is used with a tolerance parameter of $\tau_{\text{CFL}} = 0.3$ and the modifications discussed in Section 2.3. We also use an additional time-step criterion based on the maximum allowed change of the smoothing length (see Wetzstein et al. 2008, for details) with an accuracy parameter of $\tau_h = 0.15$. VINE employs a variable and time-dependent smoothing length, the number of neighbours of each particle is on average $n_{\text{neigh}} = 50$, but variations of ± 20 are allowed. The artificial viscosity of the SPH method is included in the standard way (Gingold & Monaghan 1983) with the parameters $\alpha = 1$ and $\beta = 2$ as implemented in VINE.

We performed simulations with 1 and 2 million particles in a cubic simulation domain. The particles are distributed randomly and then left to relax according to Section 3.1.1. The higher resolution compared to the test in Section 3.1 is necessary to follow the hydrodynamical shock precisely. As in the tests before, assuming a fully ionized gas with $\eta = 1.0$ and thereby using a value of $T_{\text{hot,a}} = 10^4\text{K}$ for the calculation of the sound-speed of the hot gas, does not correspond to the simulations (see equation 22). Instead a much better agreement can be achieved when the real temperature of the gas in the simulations, $T_{\text{hot,r}} = 9200\text{K}$, is used (since $\eta = 0.92$ on average in the ionized region). For this more realistic temperature the simulations are in very good agreement and converge towards the analytic solution with increasing resolution (see Fig. 5). This can also be seen in Table 1.

3.3 Performance

To test the performance of the parallel iVINE code with increasing number of processors we choose the simulation

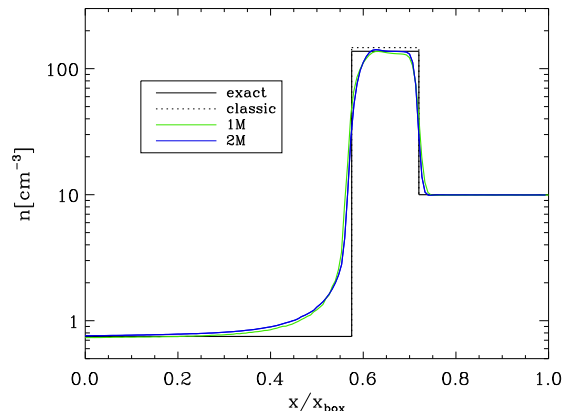


Figure 5. Number density versus position for the steady propagation of an ionizing front. The dashed line shows the classic solution, obtained by using a value of $T_{\text{hot,a}} = 10^4\text{K}$ for the hot gas. The solid line corresponds to the analytic solution for a more realistic value of $T_{\text{hot,r}} = 9200\text{K}$ for the hot gas. Blue and green lines show the simulations at different resolutions.

described in Section 4 at a later stage and compute one time-step on different numbers of CPUs. The parallel scaling of the various parts of the underlying VINE code is discussed in detail in Nelson et al. (2008). For our test, we use a SGI Altix 3700 Bx2 supercomputer. In total, the ionization uses only a few percent of the total computational time. The precise values range from 2.32% on 2 CPUs to 2.70% on 16 CPUs and 2.86% on 32 CPUs.

When refinement is used, these values change to 8.52% on 2 CPUs and 8.73% on 32 CPUs. Although the ionization takes up relatively more time in this case, the difference in the calculation time between the number of CPUs gets smaller. This is to be expected, as the refinement is calculated inside the bins and this part of the implementation is parallelized very efficiently (each bin is independent of the other bins).

This test shows that the additional cost of our implementation of ionizing radiation in SPH is always much smaller than the cost for other implemented physics, like gravity and hydrodynamics. In particular, our new ray-tracing-scheme shows a substantial speedup compared to the algorithm by Kessel-Deynet & Burkert (2000), where the path-finding alone took up about 50% of the total computational time (Kessel-Deynet 1999). Another drawback of their approach is that for every particle the optical depth is calculated along a path towards the source until a particle closer to the source with an already calculated optical depth is found. This is a highly serial approach and thus the scheme of Kessel-Deynet & Burkert (2000) does not lend itself easily to an efficient parallelization.

4 RADIATION DRIVEN IMPLOSION

As a first application of iVINE we model the radiation driven implosion of an otherwise stable molecular cloud core. This approach is very similar to Kessel-Deynet & Burkert (2003) but at ten times higher mass resolution. A marginally stable

Bonnor-Ebert sphere (BES) (Bonnor 1956) with a radial pressure profile defined by

$$\frac{1}{r^2} \frac{d}{dr} \left(\frac{r^2}{\rho} \frac{dp}{dr} \right) = -4\pi G \rho \quad (33)$$

is exposed to UV-radiation from a nearby source. The temperature of the sphere is $T = 10\text{K}$, the peak density is $n_{\text{max}} = 10^3 \text{cm}^{-3}$, and the gas is initially at rest (i.e. no turbulence). The total mass contained in the sphere is $96M_{\odot}$ and the radius is 1.6pc . We embed the sphere into cold gas (10K) with a constant density corresponding to the cutoff-density at the edge of the sphere. These simulations were performed with 2.2×10^6 particles resulting in a particle mass of $7.2 \times 10^{-5} M_{\odot}$. Self gravity is included. The cooling timescale ($t_{\text{cool}} < 0.3\text{kyr}$) is much shorter than any other timescale involved in our simulations (e.g. the crossing timescale of the hot gas is $t_{\text{hot}} \approx 70\text{kyr}$). Thus, we treat the non-ionized gas with an isothermal equation of state ($\gamma = 1$). The ionized gas is assigned a temperature according to Eq. 9 with $T_{\text{hot}} = 10^4\text{K}$ and $T_{\text{cold}} = 10\text{K}$ and then treated isothermally as well.

The artificial viscosity and the criteria for the individual time-steps are the same as in Section 3.2.1 ($\alpha = 1$, $\beta = 2$, $\tau_{\text{acc}} = 1.$, $\tau_{\text{CFL}} = 0.3$ and $\tau_{\text{h}} = 0.15$). In addition, we use a multipole acceptance criterion (MAC) for the tree based calculation of gravitational forces according to Springel et al. (2001) as implemented by Wetzstein et al. (2008) with a tree accuracy parameter of $\theta = 5 \times 10^{-4}$. The implementation of the SPH smoothing kernel and the gravitational softening length in VINE are equal at all times. The number of neighbours is set to $n_{\text{neigh}} = 50 \pm 20$. The hydrodynamical boundaries are periodic in the y- and z- direction, and open in the x-direction. This resembles the situation around a massive O-star where the material is allowed to move freely in the radial direction while at the sides similar material is existing. Gravitational forces are calculated by just taking into account the self-gravity of the gas and no external or boundary effects. This is reasonable as the total simulation time ($< 600\text{kyr}$) is much shorter than the free-fall time ($t_{\text{ff}} \approx 1.5\text{Myr}$). In the simulations the radiation is impinging from the left hand side. We perform three different simulations, differentiated by the penetration length in the surrounding medium relative to the box size $C = x_{\text{s}}/x_{\text{box}}$:

- Simulation HF (high flux):
 $F_0 = 9.0 \times 10^9 \text{photons cm}^{-2}\text{s}^{-1} \Rightarrow C \approx 1.0$
- Simulation IF (intermediate flux):
 $F_0 = 4.5 \times 10^9 \text{photons cm}^{-2}\text{s}^{-1} \Rightarrow C \approx 0.5$
- Simulation LF (low flux):
 $F_0 = 9.0 \times 10^8 \text{photons cm}^{-2}\text{s}^{-1} \Rightarrow C \approx 0.1$

This corresponds to the molecular cloud being placed inside (HF), at the border (IF) and outside (LF) of the Strömgren sphere. The evolution of the BES for all three cases is shown in Fig. 6.

4.1 Dynamical evolution

The general evolution of a simulation of this kind is as follows: As soon as the simulation starts, a R-type ionization front is driven into the medium. As it can be expected from Section 3.1.1, the front reaches the Strömgren radius x_{s} of the diffuse gas within a few recombination

timescales ($5t_{\text{rec}} \approx 5\text{kyr}$). After a sound crossing timescale ($t_{\text{hot}} \approx 70\text{kyr}$) the hot gas reacts to its change in pressure and starts to drive a shock front into the cold gas - a D-type front evolves. This front will affect the morphology of the BES. In the following we describe the individual cases in more detail.

4.1.1 Simulation HF (high flux)

Due to the high flux (see Fig. 6 first column), the R-type front is able to propagate very far into the simulation domain. A bow-like shock structure around the edge of the BES evolves ($t \approx 100\text{kyr}$). The shock front running into the denser parts of the cloud is slowed down, so that the front starts to "wrap around" the cloud. Soon the two flanks are approaching each other while the center of the shock is held back by the dense innermost region (Fig. 6 third row, first column, $t \approx 100\text{kyr}$). As the two sides finally collide an elongated filament forms which is gravitationally unstable. In Fig. 7 we show this filament at the final stage of our simulations. In comparison runs without self-gravity the two shock fronts cross each other and the cloud disperses. With the inclusion of self-gravity the filament becomes gravitational unstable and is triggered into collapse. In fact the core fragments into several objects, as will be discussed in a subsequent paper. The resolution limit according to Bate & Burkert (1997) is $n_{\text{max}} = 2 \times 10^{10} \text{cm}^{-3}$ in these simulations. As soon as this limit is reached the local Jeans mass is smaller than the mass of 100 particles and artificial fragmentation can occur. Thus, we stop the simulations at this point.

4.1.2 Simulation IF (intermediate flux)

With an intermediate flux the R-type front penetrates much less into the gaseous medium (see Fig. 6 second column). Thus, the front does not wrap around the sphere as much as in Simulation HF. As soon as the hot gas reacts to its increased temperature a flattened shock with a much smaller curvature than in Simulation HF forms. In addition, the motion in the hot gas forces the flanks on both sides of the main shock inwards, which can be seen in the velocities of the hot gas in Fig. 6 (third row, second column, $t \approx 100\text{kyr}$). These motions are due to the periodic boundaries on the upper and lower edge. Otherwise the gas could stream away freely. However these boundaries are justified by the fact that the molecular cloud is completely surrounding the O-star. In the further evolution the flanks approach each other similar to Simulation HF and the central region becomes unstable and fragments (see Fig. 7).

4.1.3 Simulation LF (low flux)

The very low flux in this case only leads to a R-front which barely reaches the sphere (see Fig. 6 third column). Therefore, the D-front starts as a nearly plane-parallel shock wave in front of the BES. This shock sweeps away much more material than in the high and intermediate flux cases, where the material is concentrated in the center. Nevertheless, as the shock propagates further the very center of the sphere gets compressed and becomes gravitationally unstable. In

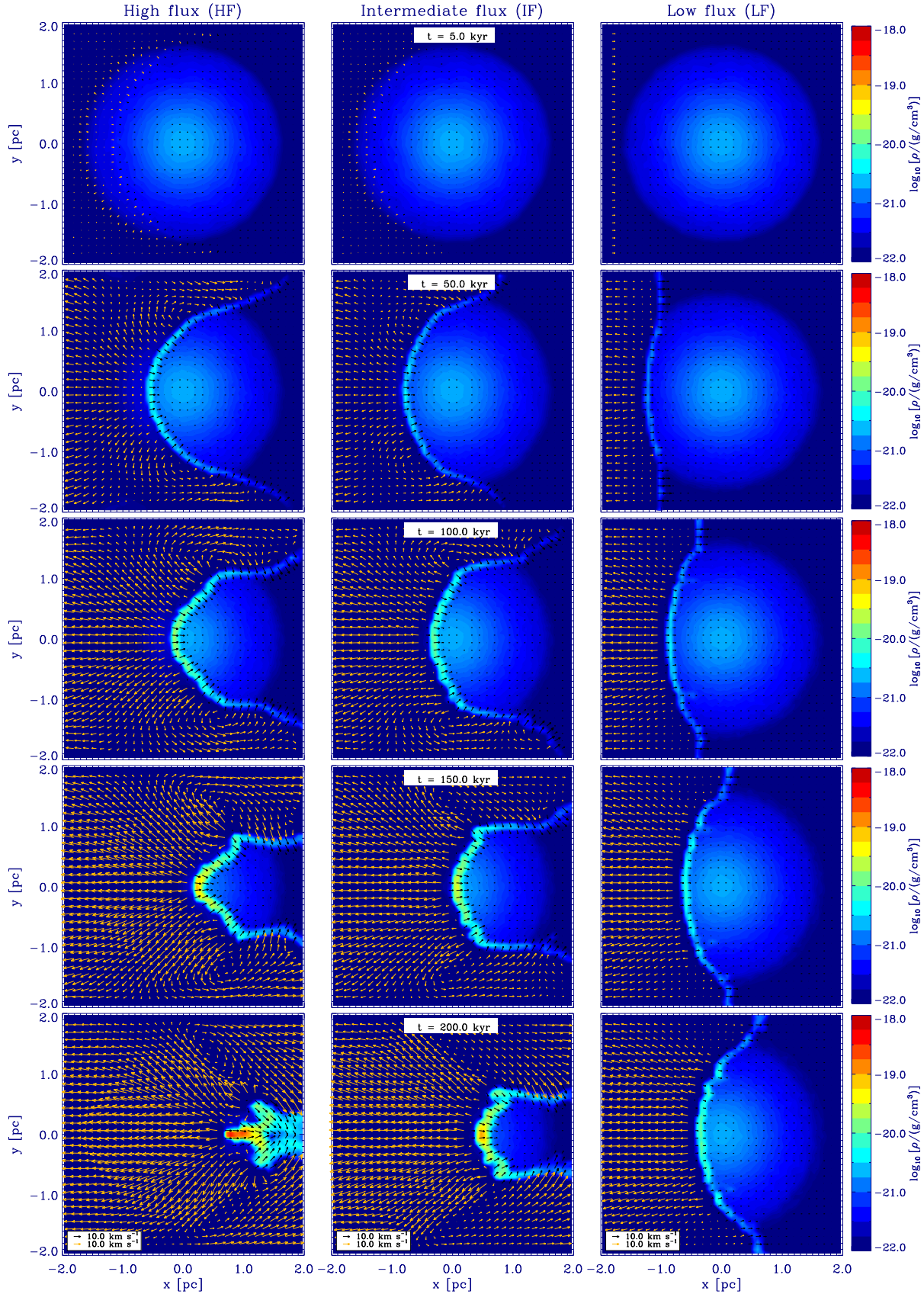


Figure 6. Time evolution of the driven collapse of a Bonnor-Ebert sphere ionized by a source with high flux (first column), intermediate flux (second column) and low flux (third column). The simulation volume is a cube with sides 4pc long, the UV-radiation is impinging from the left hand side. Color coded is the density of the central cold gas slab. Yellow arrows denote the velocities of the hot gas, black arrows the motion of the cold gas. Density and velocities are averaged across a slice of 0.125pc in the z-direction. Each row shows the

contrast to Simulations HF and IF there is no sign of fragmentation in the unstable region.

4.2 Structure, collapse timescales and final mass assembled

A close look at the final structure of the collapsing filaments of the three simulations (Fig. 7) reveals that in all three simulations the core forms at the tip of an elongated filament, which might be eroded in the future. This matches exactly the observed head to tail structure described in Section 1. The core regions have an extent of just $0.02 - 0.05\text{pc}$, which corresponds very closely to e.g. the findings of Motte & André (2001) in the Perseus star cluster. They observe 8 Class 0 protostars with compact envelopes ($R_{\text{out}} < 10^4\text{AU} \approx 0.05\text{pc}$). In addition they are denser by a factor of 3-12 than it would be expected from the standard collapse model, which would suggest densities of $n \approx 10^6\text{cm}^{-3}$ (see e.g. Walch et al. 2008, in preparation). Motte & André (2001) suggest that this higher densities are due to external disturbances initiating the collapse, which agrees very well with our simulations. Following the observations we define a core as all material with a density higher than $n_{\text{crit}} = 10^7\text{cm}^{-3}$ in a region of $R_{\text{crit}} = 0.02\text{pc}$ (which is roughly a Jeans length at a density of n_{crit}) around the peak density.

We plot the evolution of the maximum density in Fig. 8. In all three simulations after the first phase of compression by the hot gas a meta-stable phase at densities between 10^6cm^{-3} and 10^7cm^{-3} can be seen. This fits very nicely to the structure of observed cores described above. The duration of this phase depends on the initial flux (HF: 90kyr, IF: 155kyr, LF: 290kyr). In addition, we find evidence that the filaments collapse earlier in cases with a higher flux. The collapse happens at $t = 200\text{kyr}$, $t = 280\text{kyr}$ and $t = 600\text{kyr}$ in Simulation HF, IF and LF, respectively. Observations of triggered star formation tend to show the same trend (see Lee et al. 2005, Ikeda et al. 2008) - the younger the star, the further it is away from the ionizing source. This can not be explained by just attributing it to the speed of the R-type front. As seen in Section 3.1.1 the crossing time for the R-type front is of the order of a few kyr, whereas any observed age-spread is of the order of several hundred kyr. To explain this huge spread the position of the density enhancement relative to the Strömgren radius has to be considered. As we show decreasing the flux and thereby increasing the distance to the source can delay collapse and star formation by $0.08 - 0.4\text{Myr}$.

In IC 1396N Getman et al. (2007) report a T Tauri (Class II and Class III stars) population with ages $\approx 0.5 - 1\text{Myr}$. In addition, $0.3 - 0.5\text{pc}$ further away from the ionizing source HD 206267 (an O6.5f-type star), there is an embedded population of Class 0/I protostars with ages $\approx 0.1\text{Myr}$. This can be compared to our simulations where e.g. Simulation IF represents gas clumps closer to the source which start to form stars 0.3Myr earlier than Simulation LF. So at the time the embedded stars start to form in Simulation LF the stars of Simulation IF would be no longer embedded and represent the Class II/III stars population. In fact in our simulations the spread of a few hundred kyr is smaller than in the observations. This difference could be attributed to the classification of the protostars as discussed below.

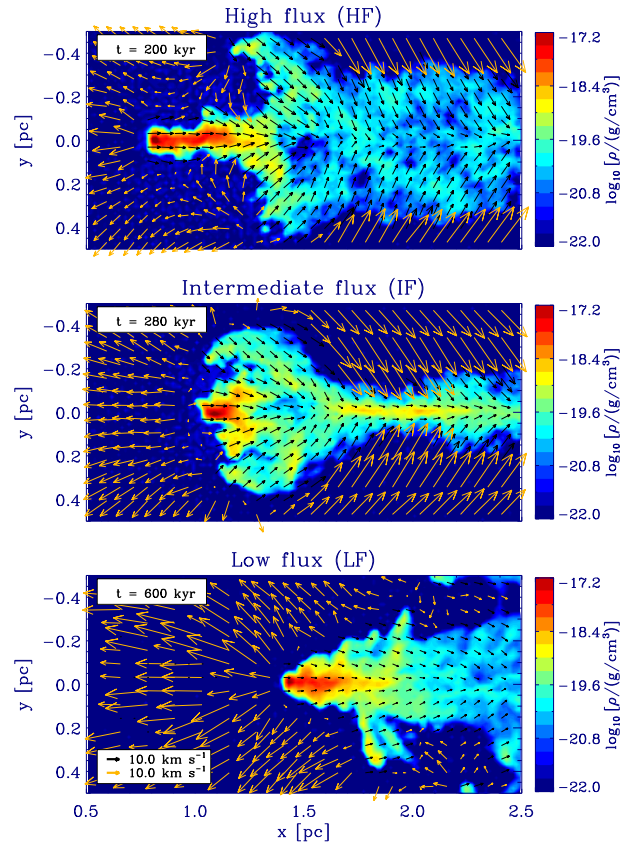


Figure 7. Final stage of the three simulations. Color coded is the density in the central slab. Yellow arrows denote the velocities of the hot gas, black arrows the motion of the cold gas. Density and velocities are averaged across a slice of 0.0625pc in the z -direction. The time of the collapse as well as the displacement of the fragment clearly depend on the initial flux. Furthermore the velocity of the cold gas (black arrows) is decreasing with decreasing flux. The core always forms at the very tip of the filament.

Besides the age-spread one can look at the velocities of the front and core. From Fig. 6 it can be seen that the shock front travels with a speed of $3 - 7\text{km/s}$, depending on the initial flux. Most observational estimates provide a front speed $< 1\text{km/s}$ (Thompson et al. 2004), leading to a difference of almost an order of magnitude between observations and simulations which has been noted before (see e.g. Getman et al. 2007). The age estimates of the YSOs are mainly based on their classification by the spectral energy distribution (SED). A Class 0/I object is deeply embedded, therefore the short micrometer wavelengths are much weaker due to absorptions in the envelope when compared to Class II/III objects. This allows for a clear distinction between both types e.g. in the IRAC $[3.6] - [4.5]$ versus $[5.8] - [8]$ color diagram as shown by Hartmann et al. (2005). We suggest that in the case of triggered star formation, the ionizing radiation could strip the envelope of a YSO, thereby unveiling the central object in short micrometer wavelengths. Thus, the observed Class II/III SED could be caused by a much younger Class 0/I protostar with a removed envelope. This would reduce the estimated age spread, thereby increasing

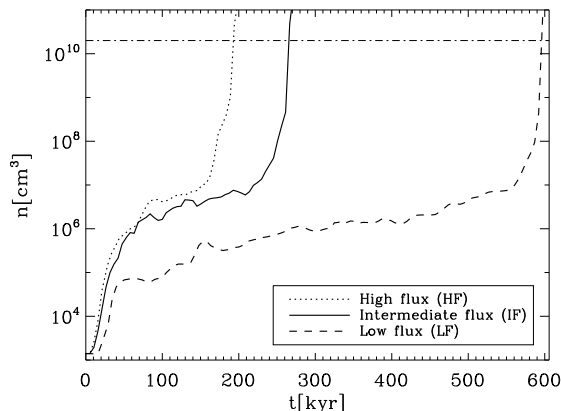


Figure 8. The maximum number density versus time for the three different simulations. In the higher flux cases HF and IF the collapse happens much earlier than in the low flux case LF. The dash-dotted line represents the resolution limit as given by Bate & Burkert (1997).

the estimated speed of the shock front and finally leading observations and simulations to agree. This assumption will be subject to further examination.

A dependence on distance is also seen for the velocities of the cold filaments (see the velocities of the cold gas (black arrows) in Fig. 7). The precise velocities of the cores in the Simulations HF, IF and LF are 8.4 km/s, 7.6 km/s and 5.1 km/s, respectively. Again, the closer the core is to the OB-association the higher is its velocity. Although this small differences are not observable yet it is worth noticing that the cores themselves have bulk velocities which are slightly higher (by about 0.5 – 1 km/s) than the rest of the filament. However, this effect may get weaker as the core gets slowed down while sweeping up the rest of the filament.

The final mass assembled does not show a dependence on the initial distance. In Simulation HF the core consists of $6.0 M_{\odot}$ in Simulation IF of $7.4 M_{\odot}$ and in Simulation LF of $2.8 M_{\odot}$. The filaments as a whole have masses of $61.5 M_{\odot}$, $75.3 M_{\odot}$ or $67.4 M_{\odot}$, respectively. It is obvious that the most effective scenario is Simulation IF. Here, the ionization encompasses most of the sphere and thus the shock front is not nearly as plane-parallel as in Simulation LF and does not sweep away as much material. On the other hand, less material gets evaporated by the ionization since the flux is lower than in Simulation HF. Overall the final masses of the collapsing cores fit the observations well. Assuming a star formation efficiency of 30% (see e.g. Lada et al. 2008), we find masses from $0.84 M_{\odot}$ to $2.2 M_{\odot}$ which agrees with the observed range from classical T Tauri up to Herbig Ae/Be stars (see e.g. Lee & Chen 2007, Snider et al. 2007).

5 SUMMARY AND DISCUSSION

We present iVINE, a new implementation of UV-radiation into the tree-SPH code VINE. It uses a plane-parallel geometry which renders the code most suitable to perform high resolution studies of the small scale effects of e.g. ionization and turbulence in the surrounding of young massive stars.

It is efficiently parallelized and very fast, as only 2%-8% of the total computational time are used for the calculation of ionization. The comparison with analytic solutions shows that iVINE treats time-dependent ionization as well as the resulting heating effects precisely and convergently.

We base our numerical implementation of ionizing radiation on several assumptions. First, we use a simplified prescription for the radiative transfer by e.g. assuming a monochromatic flux. Second, we neglect UV absorption by dust, which would lower the total UV flux. Third, we do not include a full treatment of recombination zones. In our simulations the ionized gas which gets shaded is assumed to recombine immediately. In addition, the gas in the shaded regions does not get heated by irradiation from the hot gas surrounding it. These effects require a precise time-dependent treatment of heating and cooling processes by ionization and recombination as well as a treatment for the scattering of photons. An implementation of this effects is planned in a future version of the code.

As an application we investigate radiation driven implosion of a marginally stable Bonnor-Ebert sphere. We show that these spheres are indeed driven into gravitational collapse. The resulting cores are in the observed mass range. They are more compact and a factor of ≈ 10 more dense than it would be expected in a more quiescent environment. This fact fits very well with the observations of star formation in a clustered environment. By comparing simulations with three different UV-fluxes we show that there is a clear dependence of the final mass and the age of the collapsed core on the position of the preexisting density enhancement relative to the Strömgren radius. Our findings that the onset of star formation is delayed by 0.08 – 0.4 Myr, depending on the position, are in good agreement with observations of the age spread in bright rimmed clouds. The velocity of the triggering shock is an order of magnitude higher than the observational estimates. This discrepancy has been noted before. We suggest that this can be attributed to the ionizing radiation stripping the envelope from a Class 0/I star. Thereby it might be classified as an Class II/III star, leading to an higher age-spread between the observed objects. Correcting for this effect would increase the estimated velocity of the shock front and thus lead simulations and observations towards agreement.

ACKNOWLEDGMENTS

We would like to thank the referee, James Dale, for his valuable comments on the manuscript.

This research was supported by the Deutsche Forschungsgesellschaft (DFG), SFB 375 and by the DFG cluster of excellence "Origin and Structure of the Universe".

All simulations were performed on a SGI Altix 3700 Bx2 supercomputer that was partly funded by the DFG cluster of excellence "Origin and Structure of the Universe".

REFERENCES

- Altay G., Croft R. A. C., Pelupessy I., 2008, MNRAS, 386, 1931
- Bate M. R., Burkert A., 1997, MNRAS, 288, 1060

- Bonnor W. B., 1956, MNRAS, 116, 351
- Dale J. E., Bonnell I. A., Clarke C. J., Bate M. R., 2005, MNRAS, 358, 291
- Dale J. E., Clark P. C., Bonnell I. A., 2007, MNRAS, 377, 535
- Deharveng L., Zavagno A., Caplan J., 2005, A&A, 433, 565
- Elmegreen B. G., 1998, in Woodward C. E., Shull J. M., Thronson Jr. H. A., eds, *Origins Vol. 148 of Astronomical Society of the Pacific Conference Series, Observations and Theory of Dynamical Triggers for Star Formation*. pp 150–+
- Elmegreen B. G., Kimura T., Tosa M., 1995, ApJ, 451, 675
- Elmegreen B. G., Lada C. J., 1977, ApJ, 214, 725
- Fukuda N., Hanawa T., Sugitani K., 2002, ApJ, 568, L127
- Getman K. V., Feigelson E. D., Garmire G., Broos P., Wang J., 2007, ApJ, 654, 316
- Gingold R. A., Monaghan J. J., 1983, MNRAS, 204, 715
- Gouliermis D. A., Henning T., Brandner W., Chu Y.-H., Hennekemper E., Hormuth F., 2007, ArXiv e-prints, 710, arXiv:0710.1352
- Gritschneider M., Naab T., Heitsch F., Burkert A., 2007, in Elmegreen B. G., Palous J., eds, *IAU Symposium Vol. 237 of IAU Symposium, Triggered star formation in the environment of young massive stars*. pp 246–250
- Hartmann L., Megeath S. T., Allen L., Luhman K., Calvet N., D’Alessio P., Franco-Hernandez R., Fazio G., 2005, ApJ, 629, 881
- Hester J. J., Scowen P. A., Sankrit R., Lauer T. R., Ajhar E. A., Baum W. A., Code A., Currie D. G., Danielson G. E., Ewald S. P., Faber S. M., Grillmair C. J., Groth E. J., Holtzman J. A., Hunter D. A., Kristian J., and 7 coauthors 1996, AJ, 111, 2349
- Ikedo H., Sugitani K., Watanabe M., Fukuda N., Tamura M., Nakajima Y., Pickles A. J., Nagashima C., Nagayama T., Nakaya H., Nakano M., Nagata T., 2008, AJ, 135, 2323
- Iliev I. T., Ciardi B., Alvarez M. A., Maselli A., Ferrara A., Gnedin N. Y., Mellema G., Nakamoto T., Norman M. L., Razoumov A. O., Rijkhorst E.-J., Ritzerveld J., Shapiro P. R., Susa H., Umemura M., Whalen D. J., 2006, MNRAS, 371, 1057
- Jiang Z., Yao Y., Yang J., Ando M., Kato D., Kawai T., Kurita M., Nagata T., Nagayama T., Nakajima Y., Nagashima C., Sato S., Tamura M., Nakaya H., Sugitani K., 2002, ApJ, 577, 245
- Kessel-Deynet O., 1999, PhD thesis, AA(Max-Planck-Institut für Astronomie, Königstuhl 17, D-69117 Heidelberg, Germany)
- Kessel-Deynet O., Burkert A., 2000, MNRAS, 315, 713
- Kessel-Deynet O., Burkert A., 2003, MNRAS, 338, 545
- Lada C. J., Muench A. A., Rathborne J., Alves J. F., Lombardi M., 2008, ApJ, 672, 410
- Lee H.-T., Chen W. P., 2007, ApJ, 657, 884
- Lee H.-T., Chen W. P., Zhang Z.-W., Hu J.-Y., 2005, ApJ, 624, 808
- Lefloch B., Lazareff B., 1994, A&A, 289, 559
- Mac Low M.-M., 2007, ArXiv e-prints, 711, arXiv:0711.4047
- Mac Low M.-M., Toraskar J., Oishi J. S., Abel T., 2007, ApJ, 668, 980
- Mellema G., Arthur S. J., Henney W. J., Iliev I. T., Shapiro P. R., 2006, ApJ, 647, 397
- Miao J., White G. J., Nelson R., Thompson M., Morgan L., 2006, MNRAS, 369, 143
- Motte F., André P., 2001, A&A, 365, 440
- Nelson A. F., Wetzstein M., Naab T., . 2008, ArXiv e-prints, 802
- Osterbrock D. E., 1989, *Astrophysics of gaseous nebulae and active galactic nuclei*. Research supported by the University of California, John Simon Guggenheim Memorial Foundation, University of Minnesota, et al. Mill Valley, CA, University Science Books, 1989, 422 p.
- Pawlik A. H., Schaye J., 2008, MNRAS, 389, 651
- Sandford II M. T., Whitaker R. W., Klein R. I., 1982, ApJ, 260, 183
- Shu F., 1991, *Physics of Astrophysics, Vol. II: Gas Dynamics*. Published by University Science Books, 648 Broadway, Suite 902, New York, NY 10012, 1991.
- Smith N., Egan M. P., Carey S., Price S. D., Morse J. A., Price P. A., 2000, ApJ, 532, L145
- Snider K. D., Hester J. J., Desch S. J., Healy K. R., Bally J., 2007, ArXiv e-prints, 711, arXiv:0711.1515
- Spitzer L., 1978, *Physical processes in the interstellar medium*. New York Wiley-Interscience, 1978. 333 p.
- Springel V., Yoshida N., White S. D. M., 2001, *New Astronomy*, 6, 79
- Stanke T., Smith M. D., Gredel R., Szokoly G., 2002, A&A, 393, 251
- Strömgren B., 1939, ApJ, 89, 526
- Sugitani K., Fukui Y., Mizuni A., Ohashi N., 1989, ApJ, 342, L87
- Sugitani K., Fukui Y., Ogura K., 1991, ApJS, 77, 59
- Thompson M. A., White G. J., Morgan L. K., Miao J., Fridlund C. V. M., Hultgren-White M., 2004, A&A, 414, 1017
- Walborn N. R., Maíz-Apellániz J., Barbá R. H., 2002, AJ, 124, 1601
- Wetzstein M., Nelson A. F., Naab T., Burkert A., 2008, ArXiv e-prints, 802, arXiv:0802.4245
- Yorke H. W., Bodenheimer P., Tenorio-Tagle G., 1982, A&A, 108, 25